CRYSTAL GROWTH & DESIGN

pubs.acs.org/crystal

Article

# Improving Channel Hydrate Stability via Localized Chemical Tuning of the Water Environment

Taylor A. Watts, Sara M. Niederberger, and Jennifer A. Swift*

Cite This: *Cryst. Growth Des.* 2021, 21, 5206−5214

Read Online

ACCESS | Metrics & More | Article Recommendations | Supporting Information

**ABSTRACT:** One of the long-standing challenges in working with organic hydrates in general, and channel hydrates in particular, is their propensity to lose water over time and convert (either partially or fully) to anhydrous solid forms. In this work, we demonstrate the ability to rationally increase the thermal stability of a model channel hydrate, the DNA nucleobase thymine hydrate (**TH**), through the systematic creation of lattice substitutions with 5-aminouracil (**AUr**). Mixed crystals of **TH**−**AUr** with up to 17 mol % AUr were isomorphous with the pure hydrate, confirming our molecular-level design strategy which places 5-amino groups at the one-dimensional channel surfaces. The enhanced stabilization of the water molecules afforded by the proximal 5-amino substitutions resulted in mixed crystals with significantly higher thermal stability. The magnitude of the thermal stability enhancement scaled linearly with the included **AUr** concentration, yielding **TH**−**AUr** dehydration temperatures nearly double that of the pure hydrate. Kinetic analyses and time-resolved synchrotron structural studies of process-induced dehydration of the mixed composition hydrate indicated changes in both the solid-state mechanism and the resultant anhydrous products compared to those generated from the pure hydrate. The strategy adopted herein should be applicable to other hydrate systems to rationally tune their thermal stabilities.

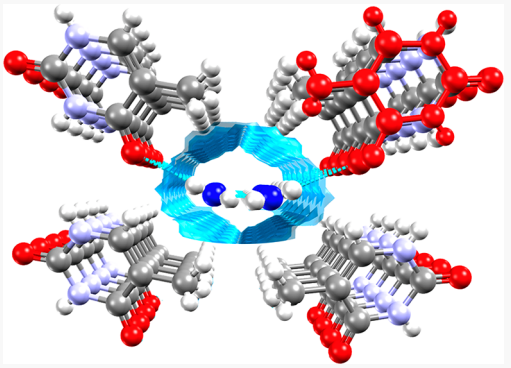



## INTRODUCTION

Organic hydrates are an important class of crystalline materials frequently encountered in the industrial processing of fine chemicals such as active pharmaceutical ingredients.[1−5] Hydrates can exhibit a broad range of stabilities, and many are susceptible to conversions to lower hydration or anhydrous states either spontaneously or in response to changes in the environmental conditions (e.g., increased temperature, decreased relative humidity). Since the physical properties of a crystalline compound depend on its structure (e.g., solubility, mechanical strength), structural transformations due to unanticipated water loss can yield unfavorable consequences.[6] Consequently, there is considerable interest in establishing a more precise understanding of the structural factors[7−14] that determine hydrate stability as well as the products that result from solid-state dehydration reactions.

Hydrates are often broadly categorized based on their water topologies—as channel hydrates, isolated hydrates, and ion-assisted hydrates.[15−19] Of these three classes, channel hydrates are often presumed to have lower thermal stabilities based on the assumption that water molecules can more easily diffuse along the water channel axis. Here we explore the possibility of expanding the thermal stability range of a channel hydrate by the introduction of site-specific lattice inclusions designed to subtly alter the local environment of the water molecules within the channel. Analogous approaches been used in other types of porous materials (e.g., metal−organic frameworks[20−23]), but to our knowledge this has not been used to systematically and intentionally tailor the properties of organic hydrates.

Thymine, one of the four DNA nucleobases, crystallizes from aqueous solution as a prototypical channel hydrate. Since the structure of thymine hydrate (**TH**) was first reported in 1961, it has been the focus of several computational and experimental investigations.[7,13,24−30] These previous studies have collectively shown that **TH** slowly dehydrates under ambient conditions (and more rapidly at elevated temperatures) yielding more than one anhydrous crystalline product. Recently, we used time-resolved *in situ* synchrotron powder X-ray diffraction (sPXRD) to monitor the subtle and dramatic structural changes that occur throughout the **TH** solid-state dehydration reaction and confirmed a diffusion mechanism was in fact operative.[30] sPXRD revealed that early water loss causes the **TH** lattice to undergo a counterintuitive "morning stretch" type motion wherein 2D layers of thymine molecules must initially increase their separation distance before

**Received:** May 12, 2021
**Revised:** July 14, 2021
**Published:** August 3, 2021

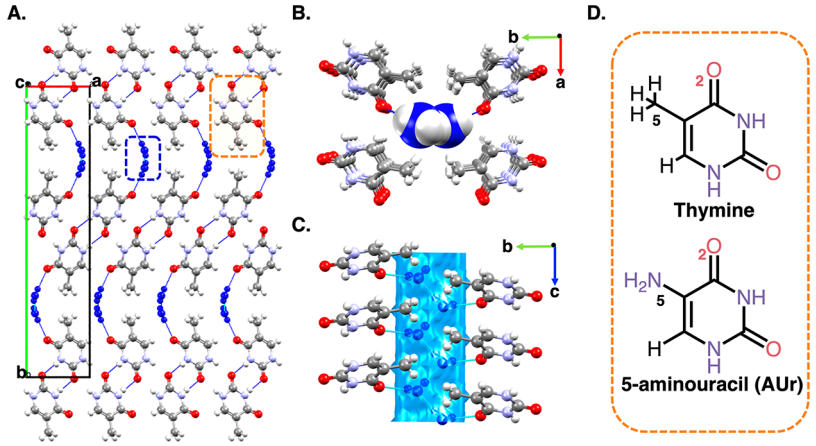


**Figure 1.** Thymine hydrate (**TH**) lattice (A) and (B) viewed down the *c*-axis, which is along the one-dimensional water channel. (C) View down the *a*-axis. Channel water molecules hydrogen bond to one another along the *c*-axis as well as to the O2 atoms of thymine molecules. (D) Molecular structures of thymine and 5-aminouracil (**AUr**).

collapsing to $Td_1$, an anhydrous form topologically similar to **TH**. Dehydration at higher temperatures or under non-isothermal heating conditions additionally yielded a second $Td_2$ phase bearing little structural similarity to the original hydrate. Notably, both $Td_1$ and $Td_2$ forms are accessible only via dehydration and are not directly from solution growth.

In this work, we demonstrate an effective strategy to improve the thermal stability of **TH** through the introduction of highly localized site-specific inclusions. Water molecules in **TH** occupy one-dimensional channels defined on two sides by the 5-methyl groups of thymine. Systematic replacement of a fraction of the 5-methyl groups with 5-amino functionalities is used as a means to increase the interaction between water molecules and the channel surface and thereby improve the thermal stability of the lattice. Herein, we report the preparation and characterization of mixed **TH** crystals with tailored 5-aminouracil (**AUr**) inclusions. The mixed crystal **TH**−**AUr** crystal compositions are isomorphous with **TH**, but the thermal stability of the material is dramatically increased as a function of **AUr** concentration. Compared to pure **TH**, the mixed crystals were also found to dehydrate via a different solid-state mechanism and yield different anhydrous products.

## EXPERIMENTAL SECTION

**Sample Preparation and Characterization.** Anhydrous thymine (T) and 5-aminouracil (**AUr**) were obtained from Sigma-Aldrich (≥99% and ≥98%, respectively) and used without further purification. Ultrapure 18.2 MΩ water from an Elga Purelab Flex system was used for all growth solutions. **TH** was prepared by heating aqueous thymine solutions (5 mg/mL), which were subsequently filtered, placed in 1 dram vials with pierced caps, and maintained at 4 °C. **TH**−**AUr**$_x$ crystals were prepared similarly, starting with mixtures of thymine and 5-aminouracil (5, 10, 15, or 20 mol % AUr) ground with a mortar and pestle. Our nomenclature for the mixed crystals references the ratio of components in the growth solution (**TH**−**AUr**$_5$, **TH**−**AUr**$_{10}$, **TH**−**AUr**$_{15}$, and **TH**−**AUr**$_{20}$). Optically transparent crystals of pure **TH** and mixed **TH**−**AUr**$_x$ crystals typically appear within 12 h. **TH** single crystals grew as elongated (010) plates bounded by medium (110) or (011) faces, with typical dimensions of 0.5 × 0.15 × 0.1 mm. Mixed **TH**−**AUr**$_x$ crystals also grew as elongated (010) plates with more variable dimensions.

Optical micrographs were obtained on an Olympus BX-50 polarizing microscope fitted with a Lumenera Xfinity 2.0 camera, an HCS302 optical hot-stage (INSTEC, Inc., Boulder, CO) and Xfinity Analyze software (Lumenera, Ontario). Powder X-ray diffraction (PXRD) data were collected at room temperature using a DUO Apex X-ray diffractometer (Cu K$\alpha$ radiation, 50 kV, 30 mA current). Lightly ground samples were placed in Kapton capillaries (Cole-Parmer, 0.0320" ID × 0.0340" OD, 12″L) with data obtained from $2\theta$ = 5−50°. PXRD data were integrated using APEX-2 software and analyzed using Panalytical X'Pert Highscore Plus software.

The AUr content and water content in **TH**−**AUr**$_x$ prepared from each component ratio were determined through $^1$H NMR and thermogravimetric analysis (TGA), respectively. $^1$H NMR of **TH**−**AUr**$_x$ crystals dissolved in DMSO-$d_6$ were collected on a 400 MHz Varian Inova spectrometer. Variable temperature TGA data were obtained in at least triplicate on a TA Instruments SDT Q600 instrument (New Castle, DE) using a nitrogen flow rate of 50 mL/min. Samples were heated at a rate of 5.0 °C/min over the temperature range 25−120 °C. All experiments used 3.0−5.0 mg of as-grown crystals in 90 $\mu$L alumina cups (TA Instruments).

**Single-Crystal Structure Determination.** X-ray diffraction data on single crystals of **TH**−**AUr**$_x$ obtained under each growth condition were collected on either a Bruker D8 Quest diffractometer equipped with a Photon 100 CMOS detector (Bruker-AXS) or a DUO Apex X-ray diffractometer equipped with an APEX II CCD detector (Bruker-AXS), each using multilayer mirror monochromated Mo Ka radiation ($\lambda$ = 0.71073 Å) at 100 K. All single-crystal structures were determined using SHELXT version 2014/5 and SHELXL-2018/3 software. All non-hydrogen atoms were modeled anisotropically, while hydrogen atoms were treated with a mixture of independent and constrained refinement parameters. The 5-amino and 5-methyl groups in **AUr** and thymine were not distinguishable based on electron density; the **AUr** occupancy was therefore fixed in each structure based on the compositions determined from solution $^1$H NMR analyses. The C−C and C−N distances were set at 1.50 (0.01) and 1.40 (0.01) Å, respectively, and the C/N atoms in the 5-position were constrained to have equal anisotropic displacement parameters. The bond angles about C3 pertaining to the 5-methyl/5-amino moieties were restrained to be 120°. Since the primary H atoms in the 5-amino group could not be located in the difference maps, they were placed in calculated positions. Similarly, H atom positions in the 5-methyl group were optimized by rotation about R−C bonds with idealized C−H, R−H, and H−H distances. Water oxygen positions were readily identified based on electron density, and their refined occupancies were consistent with TGA analyses. The H atoms on water and secondary amines were typically observable in the difference maps. Water O−H distances were restrained to be 0.88 (0.01) Å. CCDC deposition numbers: 2059761−2059764.

**Thermal Analysis and Dehydration Kinetic Studies.** Thermal transitions in **TH** and each **TH**−**AUr**$_x$ composition were evaluated using a TA Instruments differential scanning calorimeter (DSC) model Q200. DSC dehydration experiments were performed in at



https://doi.org/10.1021/acs.cgd.1c00551
Cryst. Growth Des. 2021, 21, 5206−5214

least triplicate using 3.0−5.0 mg as-grown samples in hermetically sealed aluminum pans at a heating rate of 5.0 °C/min over the temperature range 25−120 °C.

Isothermal TGA dehydration experiments were performed at 45, 50, 57, and 65 °C using the TA Instruments Q50 (New Castle, DE) using a nitrogen flow rate of 50 mL/min and a 100 μL aluminum sample pan. Samples tested (5.0−10.0 mg) were either unground, as-grown crystals, or ground in a small amount of the growth solution and vacuum-dried for 15 min prior to data collection. The linear portions of the isothermal TGA curves where the fraction dehydrated ($\alpha$) was between 0.3−0.9 were then subjected to kinetic analyses following established model-based[31,32] and model-free[9,33−35] methods. Further details regarding kinetic analyses of isothermal TGA data can be found in Supporting Information.

**Time-Resolved Synchrotron Powder X-ray Diffraction (sPXRD).** All time-resolved synchrotron data were collected on beamline 17-BM-B at the Advanced Photon Source (APS). Experiments had an X-ray beam size of 300 μm and a beam energy of 27 keV ($\lambda$ = 0.45256 Å). The beamline uses a Si (311) monochromator, a PerkinElmer a-Si Flat Panel PE1621 area detector, and an Oxford Cryosystems Cryostream 700+. Samples were ground in the mother liquor, loaded wet into 1.1 mm OD Kapton capillary (Cole-Parmer), stoppered with glass wool, and then placed in a flow cell designed for *in situ* experiments.[36] Samples were maintained under a flowing He gas atmosphere (5 mL/min) and rocked at 15° throughout the data collection. With an exposure time of 2.0 s/image (summed over 10 images), this experimental setup allowed a high Q-range sPXRD pattern to be collected every 20 s. Experiments were performed under isothermal heating conditions between 27 and 57 °C and temperature ramping conditions up to 150 °C. Image processing and integration were done with GSAS-II software[37] with further sPXRD pattern refinement and analysis done with TOPAS-V6.[38] Rietveld refinements were performed using the fundamental parameters approach.

## RESULTS AND DISCUSSION

The structure of thymine hydrate (**TH**) has been previously described in the literature,[13,24,30] but the aspects most relevant to the discussion will be briefly described here (Figure 1). In this channel hydrate, thymine molecules assemble into linear one-dimensional hydrogen-bonded tapes which closely pack in parallel into dense two-dimensional layers in the (010) plane. At the interface between layers, a lower molecular density creates a series of parallel one-dimensional channels along the ± *c*-axis which are occupied by water molecules. The original structure referred to it as a monohydrate in which 5/6 of the water sites were occupied. The channel dimensions are defined on two sides by the 5-methyl groups and above and below by the O2 and C6−H groups of thymine. Each water molecule within a given channel hydrogen bonds to up to two neighboring water molecules as well as to one thymine molecule through O2 ($O_w$···O2 = 2.84 Å). The cross-sectional diameter ($d$) of the channel at its narrowest point is approximately $d$ = 3.2 Å. With a kinetic diameter of approximately $d$ = 2.7 Å,[39] the water molecules in the **TH** channel are considered confined species. For more details about these measurements, see Supporting Information.

In previous work, we reported that the solid-state dehydration of **TH** was highly anisotropic and proceeded via a one-dimensional diffusion mechanism.[30] Through a combination of thermogravimetric kinetic studies as well as hot-stage microscopy experiments, it was clear that water loss from **TH** occurred preferentially along the channel direction. With 5-methyl groups constituting a significant fraction of the channel surface area and presumably minimal attractive interactions between water and the methyl-terminated regions, we sought to increase the affinity between water and the channel walls by systematically replacing some of the 5-methyl groups with functionalities that could provide greater stabilization. Unlike in metal−organic frameworks where postsynthetic modification strategies can be used to modify pore surfaces,[40] the narrow channel dimensions of **TH** do not allow for such methods. Rather, chemical modification to the channel walls must occur at the time of crystal assembly. Mixed hydrates of thymine and 5-aminouracil (AUr) provided a means to effectively replace some methyl groups with amino functionalities in the **TH** lattice in order to establish correlations between the water−channel interactions and the thermal properties exhibited by the material.

Solid solutions have previously been used to alter material properties in a continuous manner,[41] e.g., optoelectronic performance,[42,43] melting temperature,[44−46] and dissolution rate.[47] The efficiency and energy penalty associated with the inclusion of a secondary component in the lattice of another compound are related to many factors, one of which is the extent to which the substituting component disrupts the host lattice.[41,44,48−50] Kitaigorodsky stressed the importance of size and shape similarity in criteria for component miscibility in mixed crystals.[49,50] Most often, solid solutions are prepared using structural analogues where the secondary component is similarly sized and the functionality differs at a terminal group position (e.g., hydrogen/fluorine or methyl/chloro/bromo groups[45,51−55]), though nonterminal substitutions are also possible.[44] The similar volumes of methyl (23.5 $A^3$) and amino (19.7 $A^3$) substituents[49] and the fact that AUr does not appear to crystallize independently as a hydrate made it reasonable to explore 5-aminouracil inclusion in this system.

**Mixed TH−AUr$_x$ Crystals.** Phase pure **TH** crystallizes from supersaturated aqueous solutions (5 mg/mL) of thymine maintained at 4 °C.[13,24,30] Mixed crystals were similarly prepared from solutions of thymine and 5−20 mol % of 5-aminouracil (**AUr**) in four different stoichiometric ratios. Under these crystallization conditions, high-quality, optically transparent plates typically appeared within ∼12 h (Figure S1). Powder X-ray diffraction data of the bulk precipitate from each mixed solution composition were identical to that from pure thymine solution (Figure 2). No new diffraction lines were present in any of the mixed crystal samples, indicating that phase pure material with the same **TH** lattice was obtained at all compositions. We refer to the series of mixed crystals prepared in this work as **TH−AUr$_x$** where $x$ is the mol percent of 5-aminouracil in the growth solution.

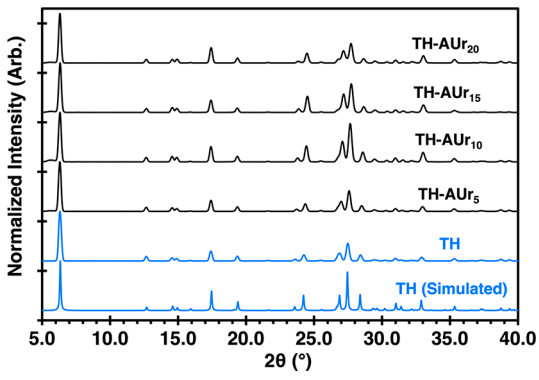


**Figure 2.** PXRD patterns of **TH−AUr$_x$** crystals grown from aqueous solutions with 5−20% **AUr** are phase pure and isostructural with **TH**.


https://doi.org/10.1021/acs.cgd.1c00551
Cryst. Growth Des. 2021, 21, 5206−5214

A linear relationship between the **AUr** concentration in the growth solution and in each **TH**−**AUr**$_x$ composition was confirmed by $^1$H NMR on dissolved crystals. Comparison of the integrated areas of the C6−H proton signal in thymine ($\delta$ = 7.24) and **AUr** ($\delta$ = 6.58) showed that approximately 85% of **AUr** present in the growth solution was included at each concentration investigated (Figure 3). **TH**−**AUr$_5$**, **TH**−**AUr$_{10}$**, **TH**−**AUr$_{15}$**, and **TH**−**AUr$_{20}$** had average AUr concentrations of 4.0(4), 8.5(3), 12.8(4), and 17.6(9) mol %, respectively. Water occupancies for each of the four **TH**−**AUr**$_x$ compositions were verified with TGA, with results indicating a water content similar to pure **TH** in all cases.

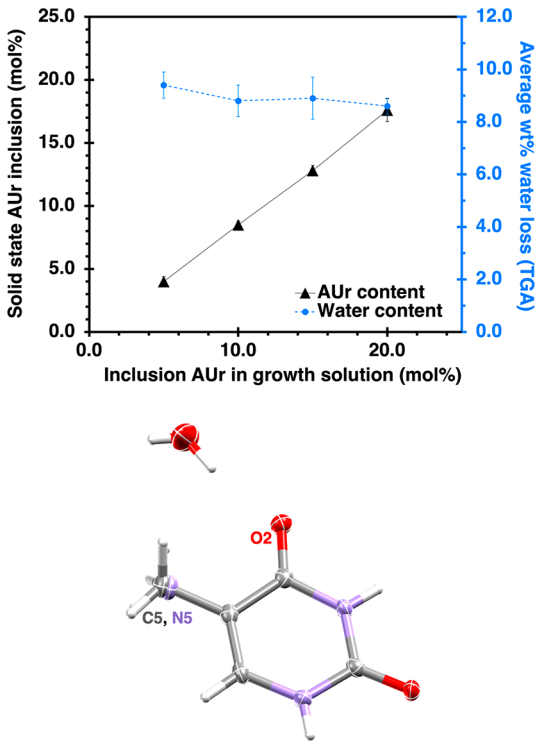


**Figure 3.** (Top) **AUr** content and water content in **TH**−**AUr**$_x$ crystals grown from aqueous solutions with 5−20% **AUr**. (Bottom) Single-crystal structure of **TH**−**AUr$_{10}$**. Included 5-aminouracil molecules adopt the same orientation as thymine in the host lattice.

Single-crystal X-ray diffraction on at least two crystals obtained from each growth solution confirmed **TH** and **TH**−**AUr**$_x$ are isomorphous. Furthermore, in each and every data set, there was no indication of disorder, indicating that the 5-amino substituent of each included AUr molecule effectively replaces one of the 5-methyl groups which define the water channel walls. We assume that the distribution of **AUr** molecules within each mixed crystal is stochastic since there was no evidence for supercell ordering in the diffraction data. Crystallographic information for each of the mixed crystal compositions is summarized in Table 1.

**Dramatically Enhanced Thermal Stability.** Collectively, the results from the X-ray diffraction, NMR, and TGA weight loss experiments indicated that the 5-amino for 5-methyl substitutions was surprisingly efficient, with the inclusion of **AUr** molecules causing minimal disruption to the parent **TH** lattice. Notably, the macroscopic plates obtained at all **TH**−**AUr**$_x$ compositions also appeared morphologically similar to pure **TH**, suggesting that perturbations to the relative growth rates along different crystallographic directions were also minimal. With the isomorphous nature of the mixed crystals confirmed, the next steps were to assess the extent to which these inclusions improved the lattice's thermal stability and whether **TH**−**AUr**$_x$ dehydration processes were affected in other identifiable ways.

When **TH** is heated under DSC conditions in a hermetically sealed pan at a heating rate of 5.0 °C/min, dehydration occurs at a maximum temperature of $T_{max}$ = 54.4 ± 0.7 °C.[30] When **TH**−**AUr**$_x$ was heated under the same conditions, significantly higher temperatures were required to affect dehydration, with the $T_{max}$ value increasing progressively with the mole fraction of included **AUr**. Representative DSC thermograms for each composition are shown in Figure 4. At even the lowest 4.0(4) mol % **AUr** inclusion levels, the endotherm in **TH**−**AUr$_5$** occurred at $T_{max}$ = 71.1 ± 0.6 °C (±95% CI) or ∼16 °C higher than **TH**. **TH**−**AUr$_{20}$** with the highest mole fraction of **AUr**, dehydrated at a remarkable $T_{max}$ = 101 ± 2 °C (±95% CI), a temperature over 45 °C higher than **TH**. The dramatic increases in thermal stability realized from site-specific modification to the **TH** lattice illustrate the enormous potential for fine-tuning the water channel properties as a means to alter thermal stability.

**Dehydration Reaction Kinetics.** Insight into the how site-specific **AUr** inclusions alter other aspects of the

**Table 1. Refined Crystallographic Parameters from Single-Crystal XRD for Mixed TH−AUr$_x$ Crystals**

| system | TH (THYMMH)[24] | TH−-AUr$_5$ | TH−AUr$_{10}$ | TH−AUr$_{15}$ | TH−AUr$_{20}$ |
|---|---|---|---|---|---|
| formula | $C_5H_6N_2O_2 \cdot 0.83(H_2O)$ | $0.96(C_5H_6N_2O_2)\ 0.04(C_4H_5N_3O_2) \cdot 0.83(H_2O)$ | $0.915(C_5H_6N_2O_2)\ 0.085(C_4H_5N_3O_2) \cdot 0.82(H_2O)$ | $0.872(C_5H_6N_2O_2)\ 0.128(C_4H_5N_3O_2) \cdot 0.83(H_2O)$ | $0.824(C_5H_6N_2O_2)\ 0.176(C_4H_5N_3O_2) \cdot 0.82(H_2O)$ |
| temperature (K) | RT | 100 | 100 | 100 | 100 |
| space group | $P2_1/c$ | $P2_1/c$ | $P2_1/c$ | $P2_1/c$ | $P2_1/c$ |
| $a$ (Å) | 6.077 | 5.9980(5) | 6.0049(6) | 6.0063(3) | 6.0120(13) |
| $b$ (Å) | 27.862 | 27.703(2) | 27.752(3) | 27.7287(14) | 27.775(7) |
| $c$ (Å) | 3.816 | 3.7251(3) | 3.7260(4) | 3.7117(2) | 3.7018(10) |
| $\beta$ (deg) | 94.32 | 93.166(3) | 93.049(2) | 93.028(2) | 92.946(10) |
| vol (Å$^3$) | 644.279 | 618.03(9) | 620.06(11) | 617.31(6) | 617.3(3) |
| $Z$ | 4 | 4 | 4 | 4 | 4 |
| $R$-factor (%) | 7.8 | 4.20 | 3.81 | 4.40 | 5.94 |
| crystal habit | plate | plate | plate | plate | plate |


https://doi.org/10.1021/acs.cgd.1c00551
Cryst. Growth Des. 2021, 21, 5206−5214

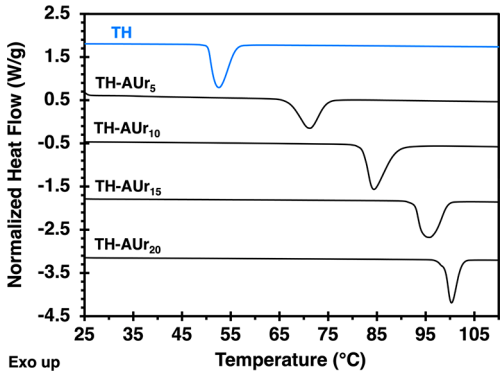


**Figure 4.** Variable temperature DSC thermograms of pure **TH** and mixed **TH**−**AUr**$_x$ crystals when heated at 5 °C/min in hermetically sealed pans. An observable increase in $T_{max}$ is accompanied by increased **AUr** concentration in the mixed crystals. With 0, 5, 10, 15, and 20 mol % of AUr in the growth solutions, average $T_{max}$ values (±95% CI) were 54.4(7), 71.1(6), 85(2), 96(3), and 101(2) °C, respectively.

dehydration reaction was gained through kinetic studies and analyses of the resulting anhydrous products. Qualitative indicators that **AUr** inclusion fundamentally altered the dehydration mechanism were initially noted in hot-stage microscopy experiments. When **TH** plates are heated, water loss via one-dimensional diffusion manifests visually as the development of opaque regions that anisotropically expand along the *c*-axis as the **TH** lattice collapses to polycrystalline anhydrous material.[30] In contrast, when **TH**−**AUr**$_x$ plates are heated more randomized opaque regions develop and multiple cracks form throughout the crystal (Figure S4). Additionally, the shape of the TGA thermograms used to determine water content in **TH** and **TH**−**AUr**$_x$ appeared qualitatively different. When heated at 5 °C/min, the **TH** weight loss curve is sigmoidal, but in **TH**−**AUr**$_x$ the weight loss occurs more gradually over a wider temperature range.

Isothermal TGA experiments performed on **TH**−**AUr**$_x$ compositions provided a more quantitative means to determine the solid-state dehydration kinetics and assess the mechanistic impacts of AUr substitutions. In a typical kinetics experiment, a sample is heated isothermally, and the fraction dehydrated, $\alpha$, is determined at each time point based on the % mass loss relative to the initial water content. Data in the linear portion of each curve from $0.3 < \alpha < 0.9$ are then fit to numerous common solid-state reaction models (Table 2). The various theoretical mathematical expressions for nucleation and growth, geometrical contraction, diffusion, and reaction-order models are based on the rate-limiting step associated with each reaction mechanism. The statistical probability of each reaction model is then evaluated based on the correlation coefficient ($R^2$) between the experimental data and each model fit. Model-free approaches can also be used to determine the reaction activation energy, $E_a$, without underlying mechanistic assumptions. (See Supporting Information for additional details.)

Previously, kinetic analyses showed **TH** dehydration occurred via a continuous one-dimensional diffusion model (D1) over a broad range of temperatures.[30] Each of the **TH**−**AUr**$_x$ compositions also underwent a smooth continuous transformation when dehydrated isothermally at 45 °C. However, when the kinetic data were fit to the reaction models in Table 2, multiple mechanisms were found to have

**Table 2. Solid-State Reaction Models and Integral Expressions Used for Kinetic Analyses**[31,32,56]

| Dehydration Models | integral equation $g(\alpha) = kt$ |
|---|---|
| Nucleation and Growth | |
| 1D growth of nuclei[a] (A2) | $(-\ln(1-\alpha))^{0.5}$ |
| 2D growth of nuclei[a] (A3) | $(-\ln(1-\alpha))^{1/3}$ |
| 3D growth of nuclei[a] (A4) | $(-\ln(1-\alpha))^{1/4}$ |
| random nucleation[b] (P1) | $\ln(\alpha/(1-\alpha)) + e^{\alpha}$ |
| Power law ($n$ = 1/2) (P2) | $\alpha^{1/2}$ |
| Power law ($n$ = 1/3) (P3) | $\alpha^{1/3}$ |
| Power law ($n$ = 1/4) (P4) | $\alpha^{1/4}$ |
| Geometrical Contraction | |
| 2D phase boundary (R2) | $1-(1-\alpha)^{1/2}$ |
| 3D phase boundary (R3) | $1-(1-\alpha)^{1/3}$ |
| Diffusion | |
| 1D diffusion (D1) | $\alpha^2$ |
| 2D diffusion (D2) | $(1-\alpha)*(\ln(1-\alpha)) + \alpha$ |
| 3D diffusion[c] (D3) | $(1-(1-\alpha)^{1/3})^2$ |
| 3D diffusion[d] (D4) | $(1-(2/3)*\alpha) - (1-\alpha)^{2/3}$ |
| Reaction Order | |
| zero-order (R1) | $\alpha$ |
| first-order (F1) | $-\ln(1-\alpha)$ |
| second-order (F2) | $(1/(1-\alpha)) - 1$ |
| third-order (F3) | $(1/2)*(((1-\alpha)^{-2}) - 1)$ |

[a]Avrami−Erofeyev equation. [b]Prout−Tompkins equation. [c]Jander equation. [d]Ginstling−Brounshtein equation

similarly good agreement. Higher-order diffusion models (D2 and D4), a three-dimensional phase boundary model (R3), and a first-order model (F1) had the highest correlation coefficients (Table S4). Although the calculated rate constant depends on the model, each of the four models showed the same clear trend in which the rate constant is inversely proportional to the AUr mol % (Table S5). In each of the four top models considered, the rate constant for **TH**−**AUr**$_{20}$ dehydration was ∼60% lower than for **TH**−**AUr**$_5$.

Isothermal dehydration was next examined in one mixed crystal composition, **TH**−**AUr**$_{10}$, at four different temperatures 45, 50, 57, and 65 °C (Figure 5). Under these conditions, the fit to 3D diffusion (D4) and first-order (F1) reaction models were similarly high (Table S6). The rate constant at each temperature was calculated, and the temperature-dependent rate constants were used to calculate the activation energy for each model. Both models yielded the same $E_a = 85 \pm 2$ kJ/mol. Kinetic data were also analyzed with model-free Friedman and

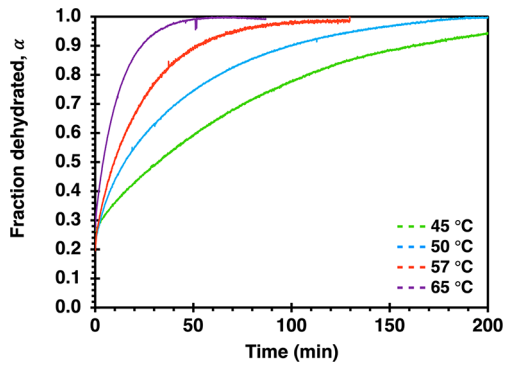


**Figure 5.** Fraction dehydrated versus time curves for **TH**−**AUr**$_{10}$ at 45 °C (green), 50 °C (blue), 57 °C (red), and 65 °C (purple). Data from $0.3 < \alpha < 0.9$ were used in kinetic analyses.


https://doi.org/10.1021/acs.cgd.1c00551
Cryst. Growth Des. 2021, 21, 5206−5214

standard methods in an effort to determine the $E_a$ apart from any mechanistic assumptions.[9,33−35] The model-free methods were also in good agreement with $E_a$ = 86 ± 9 kJ/mol (Friedman) and $E_a$ = 89 ± 9 kJ/mol (standard).

This activation energy is notable when compared to **TH** dehydration measurements determined under the same isothermal TGA conditions. Previous model-free analyses yielded an $E_a$ = 115−122 kJ/mol for this process.[30] Given its enhanced thermal stability and a greater entropic contribution, one would have expected **TH−AUr$_{10}$** to have a lower free energy than **TH**. Rationalizing the lower $E_a$ for dehydration from **TH−AUr$_{10}$** relative to **TH** required a closer look at the anhydrous products generated from the pure and mixed crystals.

**Dehydration Products and Time-Resolved Structural Changes.** As we previously reported,[30] time-resolved synchrotron PXRD studies showed that dehydration of **TH** under isothermal conditions consistently yielded at least two major anhydrous products, which we referred to as $Td_1$ and $Td_2$ (for structures, see Figure S6). Dehydration at 45 °C (0% RH) yielded $Td_1/Td_2$ in a ∼3:1 ratio; higher isothermal temperatures generally resulted in a higher mole fraction of $Td_2$. Under temperature ramping conditions and at higher temperatures, $Td_1$ was also found to transform to $Td_2$. $Td_1$ was typically not observed above ∼180 °C.

**TH−AUr$_{10}$** dehydration under identical isothermal heating conditions of 45 °C (0% RH) revealed distinct differences compared to **TH** (Figure 6). As expected, **TH−AUr$_{10}$** remained stable for much longer times (∼40 min) compared to **TH** (∼14 min), but more surprising was the fact that **TH−AUr$_{10}$** yielded $Td_1$ as the major anhydrous product. Analogous experiments on other **TH−AUr$_x$** compositions showed in each and every case that isothermal dehydration at temperatures up to 65° also yielded $Td_1$ as the major anhydrous product phase. Under temperature ramping conditions, $Td_2$ eventually did appear, but only at temperatures above ∼90 °C. This finding indicates that in addition to slowing water loss, the AUr inclusions also inhibit two different solid-state reactions—both the transformation from the hydrate to $Td_2$ as well as the polymorph transformation from $Td_1$ to $Td_2$.

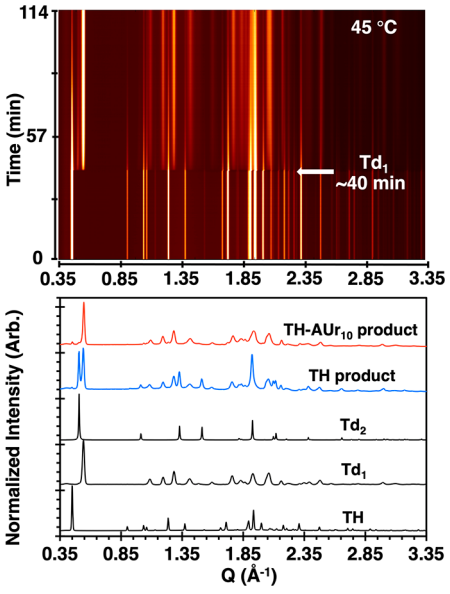


**Figure 6.** (Top) Time-resolved sPXRD contour plot tracking the dehydration of **TH−AUr$_{10}$** at 45 °C (0% RH). The plot consists of 293 sPXRD patterns collected sequentially in roughly 20 s intervals over ∼2 h. (Bottom) Comparison of the dehydration product formed from **TH−AUr$_{10}$** (red) and the dehydration product formed from **TH** (blue) under identical 45 °C (0% RH) conditions. **TH−AUr$_{10}$** dehydration yields only one anhydrous product, $Td_1$, whereas **TH** dehydration yielded two major anhydrous products, $Td_1$ and $Td_2$.

Recognition that **TH−AUr$_{10}$** and **TH** generated different anhydrous products was key to rationalizing the lower $E_a$ associated with **TH−AUr$_{10}$** dehydration. Since only one dehydration product is formed, the $E_a$ calculated from **TH−AUr$_{10}$** data cleanly describes the transformation to $Td_1$. In contrast, the $E_a$ determined from **TH** data is a convolution of two competing reactions, **TH** to $Td_1$ and **TH** to $Td_2$. (The $E_a$ associated with the $Td_1$ to $Td_2$ polymorph conversion is not accounted for in the TGA data since the reaction progress is based on weight loss.) **TH** and $Td_1$ are topologically similar and share a common one-dimensional nonpolar ribbon motif and dense (010) layer structure. In contrast, $Td_2$ has a different polar ribbon motif and layer topology. Since dehydration to $Td_1$ requires significantly less molecular reorganization and no change in either the hydrogen-bonded ribbons or aromatic stacking, it stands to reason that the $E_a$ for the **TH** to $Td_1$ reaction would be lower than the **TH** to $Td_2$ reaction.

To assess whether **AUr** inclusions affected the molecular-level reorganization from **TH−AUr$_{10}$** to $Td_1$ in other subtle ways, time-resolved sPXRD was used to track the structural changes throughout the dehydration reaction. **TH−AUr$_{10}$** was held at 27 °C (0% RH) for an extended time period (5.5 h) with a continuous collection of high-resolution patterns in 20 s intervals. Sequential refinement of the sPXRD patterns in the minutes directly preceding the appearance of $Td_1$ showed a ∼0.39% decrease in the cell volume, presumably in response to partial water loss (Figure 7). Changes in the individual cell parameters reflect the subtle changes experienced by the hydrate lattice prior to its collapse, particularly at the interfaces between the (010) layers, which are the regions most affected by water loss. Prior to the first appearance of anhydrous product, most of the lattice volume decrease in the hydrate is associated with changes in the *b*-axis and beta angle. The *a*-axis length remains essentially constant, and the *c*-axis shows only a modest decrease. Counterintuitively, the interlayer separation (*b*-axis) undergoes an initial *increase* before later decreasing at the same time the beta angle steadily decreases. These cooperative changes in the *b*-axis and beta angle presumably enable the 5-X substituents on the corrugated (010) planes to move past one another. This same "morning stretch" type motion was also identified in time-resolved **TH** dehydration studies. While altering the size and chemistry of the 5-X substituents could affect the energetics of this morning stretch motion, the magnitude of the changes in **TH−AUr$_{10}$** cell parameters were quite similar to those previously observed in **TH**. Relatedly, the thermal expansion in **TH** and **TH−AUr$_{10}$** over a temperature range from 25−57 °C was also comparable in magnitude (Figure S8). On the basis of these data, we conclude that while **AUr** inclusions have a significant effect on water mobility in the channel, they do not appear to significantly alter the thymine motions that lead to $Td_1$.

## CONCLUSION

In summary, we have demonstrated how large gains in thermal stability can be realized in a channel hydrate by molecular-level engineering of mixed crystals with site-specific inclusions that


https://doi.org/10.1021/acs.cgd.1c00551
Cryst. Growth Des. 2021, 21, 5206−5214

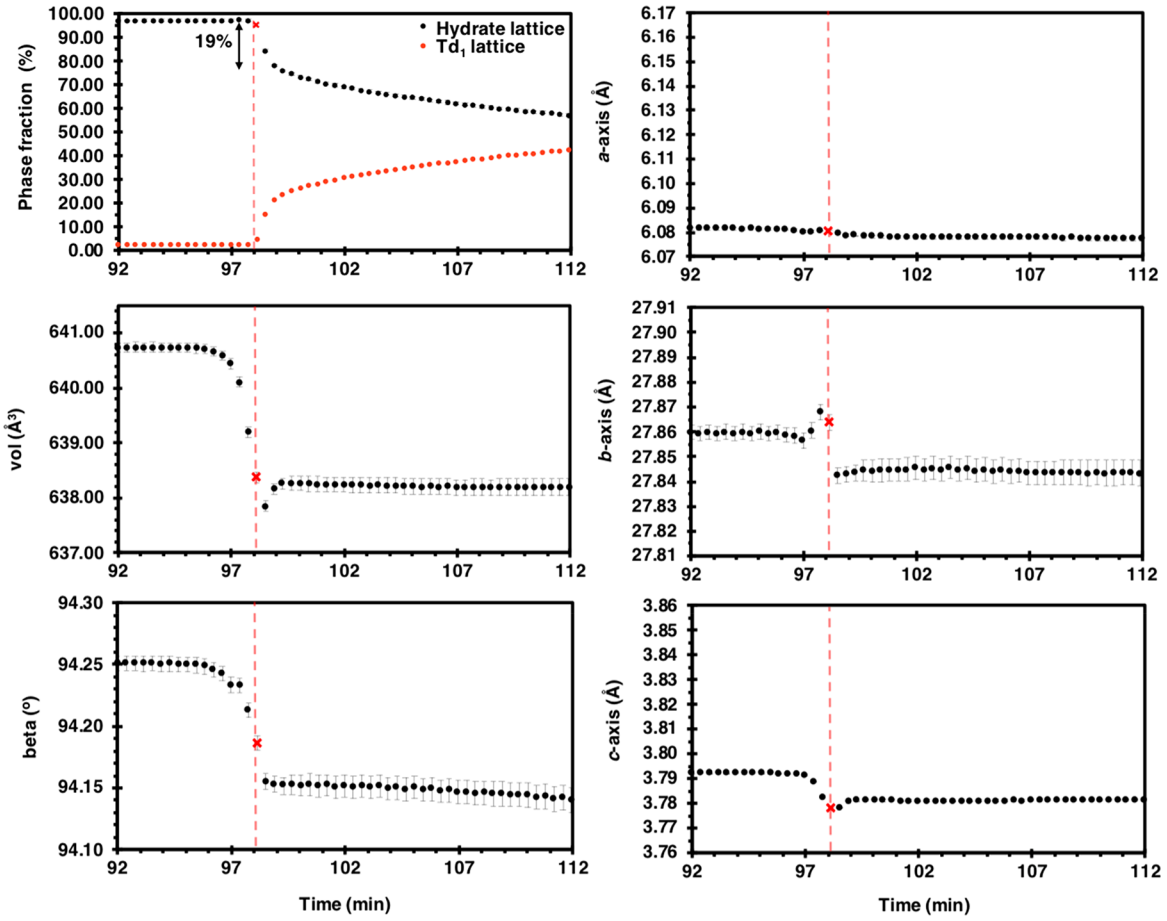


**Figure 7.** Unit cell parameters obtained from sequential refinement of 53 sPXRD patterns between 92 and 112 min when **TH−AUr$_{10}$** was heated isothermally at 27 °C (0% RH) for 5.5 h. The point in red corresponds to the first powder pattern where diffraction lines corresponding to the dehydration product are observed. The subtle changes in the hydrate cell parameters which precede the appearance of anhydrate indicate that the lattice is able to adapt to some fractional amount of water loss prior to its collapse.

subtly alter the local water environment. The systematic replacement of 5−20% of the thymine molecules in the hydrate lattice with 5-aminouracil correlated with significant increases in the thermal stability and dehydration temperature up to 40° higher than the pure materials without disruption to the overall lattice structure. Reaction kinetic studies and time-resolved synchrotron PXRD studies in combination allowed for a molecular-level understanding of how the 5-aminouracil inclusions alter the course of process-induced dehydration. We believe our approach to tuning channel hydrate properties via molecular-level tuning of the water channel surface is a powerful and potentially generalizable method that should be applicable to other hydrate systems to improve their thermal stabilities. In the context of polymorph discovery, this strategy also offers the opportunity to alter the structure and/or distribution of the anhydrous forms generated via process-induced dehydration methods.

## ■ ASSOCIATED CONTENT

### Supporting Information

The Supporting Information is available free of charge at https://pubs.acs.org/doi/10.1021/acs.cgd.1c00551.

Micrographs, TGA, DSC, NMR, kinetics tables, synchrotron PXRD (PDF)

### Accession Codes

CCDC 2059761−2059764 contain the supplementary crystallographic data for this paper. These data can be obtained free of charge via www.ccdc.cam.ac.uk/data_request/cif, or by emailing data_request@ccdc.cam.ac.uk, or by contacting The Cambridge Crystallographic Data Centre, 12 Union Road, Cambridge CB2 1EZ, UK; fax: +44 1223 336033.

## ■ AUTHOR INFORMATION


### Corresponding Author

**Jennifer A. Swift** − *Department of Chemistry, Georgetown University, Washington, D.C. 20057-1227, United States;* orcid.org/0000-0002-8011-781X; Email: jas2@georgetown.edu

### Authors

**Taylor A. Watts** − *Department of Chemistry, Georgetown University, Washington, D.C. 20057-1227, United States*

**Sara M. Niederberger** − *Department of Chemistry, Georgetown University, Washington, D.C. 20057-1227, United States*

Complete contact information is available at: https://pubs.acs.org/10.1021/acs.cgd.1c00551


### Notes

The authors declare no competing financial interest.



https://doi.org/10.1021/acs.cgd.1c00551
*Cryst. Growth Des.* 2021, 21, 5206−5214

## ■ ACKNOWLEDGMENTS

The authors gratefully acknowledge financial support from the Henry Luce Foundation (TAW Clare Boothe Luce Predoctoral Fellowship) and the National Science Foundation (DMR 1609541 and 2004435). We thank Jeffery Bertke for his help with crystallographic analysis and Andrey Yakovenko and Weiquian Xu for their assistance with collecting synchrotron data. This research used resources of the Advanced Photon Source, a U.S. Department of Energy (DOE) Office of Science User Facility operated for the DOE Office of Science by Argonne National Laboratory under Contract No. DE-AC02-06CH11357.

## ■ REFERENCES

(1) Griesser, U. J. The Importance of Solvates. In *Polymorphism*; Hilfiker, R., Ed.; Wiley, 2006; pp 211−233..
(2) Stahly, G. P. Diversity in Single- and Multiple-Component Crystals. The Search for and Prevalence of Polymorphs and Cocrystals. *Cryst. Growth Des.* **2007**, *7* (6), 1007−1026.
(3) van de Streek, J.; Motherwell, S. New software for searching the Cambridge Structural Database for solvated and unsolvated crystal structures applied to hydrates. *CrystEngComm* **2007**, *9*, 55−64.
(4) Görbitz, C. H.; Hersleth, H.-P. On the inclusion of solvent molecules in the crystal structures of organic compounds. *Acta Crystallogr., Sect. B: Struct. Sci.* **2000**, *B56*, 526−534.
(5) Werner, J. E.; Swift, J. A. Data mining the Cambridge Structural Database for hydrate−anhydrate pairs with SMILES strings. *CrystEngComm* **2020**, *22*, 7290−7297.
(6) Pudipeddi, M.; Serajuddin, A. T. M. Trends in Solubility of Polymorphs. *J. Pharm. Sci.* **2005**, *94* (5), 929−939.
(7) Perrier, P. R.; Byrn, S. R. Influence of Crystal Packing on the Solid-State Desolvation of Purine and Pyrimidine Hydrates: Loss of Water of Crystallization from Thymine Monohydrate, Cytosine Monohydrate, 5-Nitrouracil Monohydrate, and 2′-Deoxyadenosine Monohydrate. *J. Org. Chem.* **1982**, *47*, 4671−4676.
(8) Brittain, H. G.; Morris, K. R.; Boerrigter, S. X. M. Structural Aspects of Solvatomorphic Systems. In *Polymorphism in Pharmaceutical Solids*, 2nd ed.; Brittain, H. G., Ed.; Taylor & Francis, 2009; pp 233−281.
(9) Zhou, D.; Schmitt, E. A.; Zhang, G. G. Z.; Law, D.; Wight, C. A.; Vyazovkin, S.; Grant, D. J. W. Model-free treatment of the dehydration kinetics of nedocromil sodium trihydrate. *J. Pharm. Sci.* **2003**, *92*, 1367−1376.
(10) Braun, D. E.; Koztecki, L. H.; Mcmahon, J. A.; Price, S. L.; Reutzel-Edens, S. M. Navigating the Waters of Unconventional Crystalline Hydrates. *Mol. Pharmaceutics* **2015**, *12*, 3069−3088.
(11) Lee, J.; Kim, D.; Park, J.; Kim, E. E.; Lah, M. S.; Kim, A. Pseudopolymorphs of LB30870, a Direct Thrombin Inhibitor: One-Dimensional Solvent Channel Structures Explain Reversible Hydration/Dehydration. *Cryst. Growth Des.* **2018**, *18*, 95−104.
(12) Braun, D. E.; Griesser, U. J. Stoichiometric and Non-stoichiometric Hydrates of Brucine. *Cryst. Growth Des.* **2016**, *16*, 6111−6121.
(13) Braun, D. E.; Gelbrich, T.; Wurst, K.; Griesser, U. J. Computational and Experimental Characterization of Five Crystal Forms of Thymine: Packing Polymorphism, Polytypism/Disorder, and Stoichiometric 0.8-Hydrate. *Cryst. Growth Des.* **2016**, *16*, 3480−3496.
(14) Kiang, Y.-H.; Cheung, E.; Stephens, P. W.; Nagapudi, K. Structural Studies of a Non-Stoichiometric Channel Hydrate Using High Resolution X-ray Powder Diffraction, Solid-State Nuclear Magnetic Resonance, and Moisture Sorption Methods. *J. Pharm. Sci.* **2014**, *103*, 2809−2818.
(15) Morris, K. R. Structural Aspects of Hydrates and Solvates. In *Polymorphism in Pharmaceutical Solids*; Brittain, H. G., Ed.; Marcel Dekker, Inc.: New York, 1999; pp 125−181.
(16) Morris, K. R.; Rodriguez-Hornado, N. Hydrates. In *Encyclopedia of Pharmaceutical Technology*, Swarbrick, J., Boylan, J. C., Eds.; Dekker: New York, 1993; *Vol. 7*, pp 393−440.
(17) Khankari, R. K.; Grant, D. J. W. Pharmaceutical hydrates. *Thermochim. Acta* **1995**, *248*, 61−79.
(18) Infantes, L.; Fábián, L. s.; Motherwell, W. D. S. Organic crystal hydrates: what are the important factors for formation. *CrystEngComm* **2007**, *9*, 65.
(19) Gillon, A. L.; Feeder, N.; Davey, R. J.; Storey, R. Hydration in Molecular CrystalsA Cambridge Structural Database Analysis. *Cryst. Growth Des.* **2003**, *3* (5), 663−673.
(20) Burtch, N. C.; Jasuja, H.; Walton, K. S. Water Stability and Adsorption in Metal−Organic Frameworks. *Chem. Rev.* **2014**, *114*, 10575−10612.
(21) Akiyama, G.; Matsuda, R.; Sato, H.; Hori, A.; Takata, M.; Kitagawa, S. Effect of functional groups in MIL-101 on water sorption behavior. *Microporous Mesoporous Mater.* **2012**, *157*, 89−93.
(22) Biswas, S.; Ahnfeldt, T.; Stock, N. New Functionalized Flexible Al-MIL-53-X (X = − Cl, -Br, -CH3, -NO2, -(OH)2) Solids: Syntheses, Characterization, Sorption, and Breathing Behavior. *Inorg. Chem.* **2011**, *50* (19), 9518−9526.
(23) Reinsch, H.; van der Veen, M. A.; Gil, B.; Marszalek, B.; Verbiest, T.; de Vos, D.; Stock, N. Structures, Sorption Characteristics, and Nonlinear Optical Properties of a New Series of Highly Stable Aluminum MOFs. *Chem. Mater.* **2013**, *25* (1), 17−26.
(24) Gerdil, R. The crystal structure of thymine monohydrate. *Acta Crystallogr.* **1961**, *14*, 333−344.
(25) Ozeki, K.; Sakabe, N.; Tanaka, J. The crystal structure of thymine. *Acta Crystallogr., Sect. B: Struct. Crystallogr. Cryst. Chem.* **1969**, *25*, 1038−1045.
(26) Portalone, G.; Bencivenni, L.; Colapietro, M.; Pieretti, A.; Ramondo, F.; Møller, J.; Senning, A.; Yao, X.-K.; Wang, H.-G.; Tuchagues, J.-P.; Ögren, M. The Effect of Hydrogen Bonding on the Structures of Uracil and Some Methyl Derivatives Studied by Experiment and Theory. *Acta Chem. Scand.* **1999**, *53*, 57−68.
(27) Barnett, S. A.; Hulme, A. T.; Issa, N.; Lewis, T. C.; Price, L. S.; Tocher, D. A.; Price, S. L. The observed and energetically feasible crystal structures of 5-substituted uracils. *New J. Chem.* **2008**, *32*, 1761.
(28) Chennuru, R.; Muthudoss, P.; Ramakrishnan, S.; Mohammad, A. B.; Ravi Chandra Babu, R.; Mahapatra, S.; Nayak, S. K. Preliminary studies on unusual polymorphs of thymine: Structural comparison with other nucleobases. *J. Mol. Struct.* **2016**, *1120*, 86−99.
(29) Ahlqvist, M. U. A.; Taylor, L. S. Water dynamics in channel hydrates investigated using H/D exchange. *Int. J. Pharm.* **2002**, *241*, 253−261.
(30) Watts, T. A.; Miehls, E. K.; Swift, J. A. Time-Resolved Cooperative Motions in the Solid-State Dehydration of Thymine Hydrate. *Cryst. Growth Des.* **2020**, *20*, 7941−7950.
(31) Khawam, A.; Flanagan, D. R. Solid-state kinetic models: Basics and mathematical fundamentals. *J. Phys. Chem. B* **2006**, *110*, 17315−17328.
(32) Khawam, A.; Flanagan, D. R. Basics and Applications of Solid-State Kinetics: A Pharmaceutical Perspective. *J. Pharm. Sci.* **2006**, *95*, 472−498.
(33) Khawam, A.; Flanagan, D. R. Role of isoconversional methods in varying activation energies of solid-state kinetics I. Isothermal kinetic studies. *Thermochim. Acta* **2005**, *429*, 93−102.
(34) Koradia, V.; De Diego, H. L.; Elema, M. R.; Rantanen, J. Integrated approach to study the dehydration kinetics of nitrofurantoin monohydrate. *J. Pharm. Sci.* **2010**, *99*, 3966−3976.
(35) Friedman, H. L. New methods for evaluating kinetic parameters from thermal analysis data. *J. Polym. Sci., Part B: Polym. Lett.* **1969**, *7*, 41−46.
(36) Chupas, P. J.; Chapman, K. W.; Kurtz, C.; Hanson, J. C.; Lee, P. L.; Grey, C. P. A versatile sample-environment cell for non-ambient X-ray scattering experiments. *J. Appl. Crystallogr.* **2008**, *41*, 822−824.



https://doi.org/10.1021/acs.cgd.1c00551
*Cryst. Growth Des.* 2021, 21, 5206−5214

(37) Toby, B. H.; Von Dreele, R. B. GSAS-II: the genesis of a modern open-source all purpose crystallography software package. *J. Appl. Crystallogr.* **2013**, *46*, 544−549.
(38) Coelho, A. A. *TOPAS-64*; Bruker AXS, Coelho Software: Brisbane, 2016.
(39) Ismail, A. F.; Khulbe, K. C.; Matsuura, T. *Gas Separation Membranes: Polymeric and Inorganic*; Springer International Publishing: 2015.
(40) Wang, Z.; Cohen, S. M. Postsynthetic modification of metal−organic frameworks. *Chem. Soc. Rev.* **2009**, *38* (5), 1315−1329.
(41) Lusi, M. A rough guide to molecular solid solutions: design, synthesis and characterization of mixed crystals. *CrystEngComm* **2018**, *20* (44), 7042−7052.
(42) Shao, Y.; Yang, Y. White organic light-emitting diodes prepared by a fused organic solid solution method. *Appl. Phys. Lett.* **2005**, *86* (7), 073510.
(43) Shao, Y.; Yang, Y. Organic Solid Solutions: Formation and Applications in Organic Light-Emitting Diodes. *Adv. Funct. Mater.* **2005**, *15* (11), 1781−1786.
(44) Schur, E.; Nauha, E.; Lusi, M.; Bernstein, J. Kitaigorodsky Revisited: Polymorphism and Mixed Crystals of Acridine/Phenazine. *Chem. - Eur. J.* **2015**, *21* (4), 1735−1742.
(45) Braga, D.; Grepioni, F.; Maini, L.; Polito, M.; Rubini, K.; Chierotti, M. R.; Gobetto, R. Hetero-Seeding and Solid Mixture to Obtain New Crystalline Forms. *Chem. - Eur. J.* **2009**, *15* (6), 1508−1515.
(46) Brandel, C.; Amharar, Y.; Rollinger, J. M.; Griesser, U. J.; Cartigny, Y.; Petit, S.; Coquerel, G. Impact of Molecular Flexibility on Double Polymorphism, Solid Solutions and Chiral Discrimination during Crystallization of Diprophylline Enantiomers. *Mol. Pharmaceutics* **2013**, *10* (10), 3850−3861.
(47) Brader, M. L.; Sukumar, M.; Pekar, A. H.; McClellan, D. S.; Chance, R. E.; Flora, D. B.; Cox, A. L.; Irwin, L.; Myers, S. R. Hybrid insulin cocrystals for controlled release delivery. *Nat. Biotechnol.* **2002**, *20* (8), 800−804.
(48) York, P.; Grant, D. J. W. A disruption index for quantifying the solid state disorder induced by additives or impurities. I. Definition and evaluation from heat of fusion. *Int. J. Pharm.* **1985**, *25* (1), 57−72.
(49) Kitaigorodsky, A. I. Structure of Crystals. In *Molecular Crystals and Molecules*; Academic Press Inc.: 1973; *Vol. 29*, pp 1−133.
(50) Kitaigorodskii, A. I. *Mixed Crystals*; Springer-Verlag: Berlin, 1984; *Vol. 33*.
(51) Braun, D. E.; Kahlenberg, V.; Griesser, U. J. Experimental and Computational Hydrate Screening: Cytosine, 5-Flucytosine, and Their Solid Solution. *Cryst. Growth Des.* **2017**, *17*, 4347−4364.
(52) Paul, M.; Chakraborty, S.; Desiraju, G. R. Six-Component Molecular Solids: ABC[D1−(x+y)ExFy]2. *J. Am. Chem. Soc.* **2018**, *140* (6), 2309−2315.
(53) Bučar, D.-K.; Sen, A.; Mariappan, S. V. S.; MacGillivray, L. R. A [2 + 2] cross-photodimerisation of photostable olefins via a three-component cocrystal solid solution. *Chem. Commun.* **2012**, *48* (12), 1790−1792.
(54) Theocharis, C. R.; Desiraju, G. R.; Jones, W. The use of mixed crystals for engineering organic solid-state reactions: application to benzylbenzylidenecyclopentanones. *J. Am. Chem. Soc.* **1984**, *106* (12), 3606−3609.
(55) Dabros, M.; Emery, P. R.; Thalladi, V. R. A Supramolecular Approach to Organic Alloys: Cocrystals and Three- and Four-Component Solid Solutions of 1,4-Diazabicyclo[2.2.2]octane and 4-X-Phenols (X = Cl, CH3, Br). *Angew. Chem., Int. Ed.* **2007**, *46* (22), 4132−4135.
(56) Galwey, A. K. Structure and order in thermal dehydrations of crystalline solids. *Thermochim. Acta* **2000**, *355*, 181−238.



https://doi.org/10.1021/acs.cgd.1c00551
*Cryst. Growth Des.* 2021, 21, 5206−5214